Available online at www.sciencedirect.com
SCIENCE DIRECT®
Journal of Solid State Chemistry 178 (2005) 2838–2845
JOURNAL OF SOLID STATE CHEMISTRY
www.elsevier.com/locate/jssc

Synthesis and crystallization of macroporous hydroxyapatite

S. Madhavi*, C. Ferraris, T.J. White

School of Materials Science and Engineering, Nanyang Technological University, Block N4.1-B4-10, 50 Nanyang Avenue, Singapore 639798, Singapore

Received 10 April 2005; received in revised form 10 June 2005; accepted 11 June 2005

Abstract

Macroporous hydroxyapatite $Ca_{10}(PO_4)_6(OH)_2$ was synthesized using ordered polystyrene sphere templates that were impregnated with a calcium phosphate precursor solution which was allowed to solidify followed by sintering from 500 to 1000 °C in flowing oxygen to remove the polymer and crystallize the phosphates. Using a combination of diffraction and imaging the face-centered cubic macroporous framework was shown to have pore diameters of 0.8–0.9 μm and to be composed of hydroxyapatite (80–98 wt%) and X-ray diffraction amorphous material (14–55%), the proportions dependent on the duration and temperature of heat treatment. At lower sintering temperatures the HAp is calcium deficient. Ion exchange of calcium by cadmium demonstrated the potential of this material for hazardous waste remediation.

Keywords: Hydroxyapatite; Macroporous; 3DOM; Ion-exchange

1. Introduction

There is an emerging interest in three-dimensionally ordered macroporous (3DOM) [1–9] materials derived from close-packed templates of monodisperse spheres (silica or polystyrene) as membranes [10,11], catalysts [12,13] and biomaterials [14–16] where specific combinations of high porosity, low density and large effective surface area are required. Ecomaterials applications have received less attention, although thiol-functionalized macroporous titania and zirconia for the adsorption of heavy metals from waste liquors has been described [17]. In this case, a high level of thiol coverage was achieved, but less than stoichiometric adsorption took place due to limited accessibility of the dissolved metals to the thiol groups attached to the interior walls. Alternatively 3DOM ecomaterials can be synthesized where the walls themselves are the functional materials that directly capture heavy metals by surface sorption or ion exchange [18–24]. $Ca_{10}(PO_4)_6(OH)_2$ hydroxyapatite (HAp) is a candidate wall compound, that in powdered form, has been the subject of numerous studies (in particular for Cd and Pb waste remediation) and which immobilizes metals through dissolution-precipitation or ion-exchange reactions [18–35]. While it is evident these fixation reactions can be enhanced by fabricating high surface area frameworks that facilitate mass transfer [19,22,25,26] the application of 3DOM HAp for inorganic ion immobilization has not been considered, although the potential benefits include a facile diffusion pathway for waste liquor transport and greater access to the active ion-exchangeable crystallographic sites.

Polyphase 3DOM calcium phosphates have been synthesized as matrices for in vitro antibiotic drug release [15] where HAp co-exists with β-tricalcium phosphates (β-TCP) and other calcium phosphates. While mixed phase assemblages are beneficial for biomedical applications, efficient toxic metal stabilization requires macroporous networks made up primarily of crystalline HAp. For both biomaterials and ecomaterials, 3DOM HAp functionality will be altered by X-ray amorphous phases, whose high diffusion coefficients and unique chemistries will modify interactions with body fluid and waste streams. However, quantitative phase analysis to establish the crystalline and

*Corresponding author. Fax: +65 67909081.
E-mail address: madhavi@ntu.edu.sg (S. Madhavi).

0022-4596/$ - see front matter © 2005 Elsevier Inc. All rights reserved.
doi:10.1016/j.jssc.2005.06.039

amorphous contents of 3DOM materials are not generally reported even though low-temperature synthesis may favor partial crystallization.

In this paper, we describe the synthesis and characterization of near single-phase 3DOM HAp. The evolution of crystallinity and macroporosity as a function of sintering temperature and time were monitored by scanning (SEM) and transmission electron microscopy (TEM). Rietveld analysis of powder X-ray diffraction (XRD) data allowed the examination of HAp nonstoichiometry and the assessment of amorphicity. Analytical TEM confirmed a reversible ion-exchange reaction of calcium by cadmium in 3DOM HAp.

2. Experimental methods

2.1. Materials

Monodispersed polystyrene latex microsphere suspensions with mean diameter of 1.0 μm and a size distribution of ±3% purchased from Duke Scientific Corporation (USA) were used as received. Other reagents were $Ca(NO_3)_2 \cdot 4H_2O$ (98.5%, BDH), orthophosphoric acid H_3PO_4 (99%, Merck), absolute ethanol (Merck), and distilled water (MilliQ water system from Millipore).

2.2. Synthesis of macroporous HAp

Well-ordered centimeter-scale close packed polymer templates were prepared by spinning the suspensions for 48 h at 900 rpm followed by air drying. The templates were strengthened by annealing for 15–20 min at 100 °C before infiltration of the void space to create necks which provide intersphere connections that strengthen the template and prevent disintegration in the precursor solution. This step is critical as excessive sintering fuses the spheres and closes diffusion pathways prohibiting further infiltration. The precursor solution was made by adding stoichiometric amounts of 0.8 M H_3PO_4 in absolute ethanol to 1.64 M $Ca(NO_3)_2 \cdot 4H_2O$ in water (Ca/P ratio = 1.67) under vigorous stirring. The templates were soaked in this solution for 30 min to allow penetration by capillary action. While both starting chemicals were readily soluble in water, ethanolic solutions were preferable because the template surfaces were wetted more effectively without disturbing the close packed arrangement. Finally, the excess solution was removed by vacuum filtration with repeated infiltration ensuring complete filling of the voids by capillary action. The infiltered template was dried in a vacuum dessicator for 24 h to accelerate the liquid to solid transformation of the walls. The oxide-polymer composites were sintered in a tube furnace under flowing oxygen at 400 °C for 3 h at a heating rate of 1 °C/min to minimize carbon residue, followed by calcination between 500 and 1000 °C for 1 h (heating rate: 2 °C/min). Different sample batches were heated at 500 and 700 °C for 6 h under the same conditions.

2.3. Characterization

Secondary electron images (SEI) were obtained using a JEOL JSM-5310LV scanning microscope operating at accelerating voltages of 10, 15 or 20 keV to control specimen charging. The samples were gold coated using an SPI Supplies (USA) sputter coater and fixed by double-sided carbon tape to an aluminum sample holder. Powder X-ray diffraction (XRD) patterns of the macroporous powders were collected using a Siemens D5005 diffractometer with Cu$K\alpha$ radiation and step-scanned over the 2θ range 10–80° at intervals of 0.02°, with a step time of 14 s leading to a total collection time of 13.6 h. XRD patterns were obtained from each batch of samples with and without a standard alumina spike (20 wt% NIST SRM 676) [36] to determine the crystalline and amorphous content, respectively [37–42]. Infrared spectral studies in the range 400–4000 cm^{-1} were recorded with a Perkin Elmer FTIR Spectrum 2000 with spectral resolution of 4 cm^{-1} using translucent pellets prepared by mixing 3DOM powders with KBr. Transmission, scanning transmission and analytical electron microscopic (TEM-STEM and AEM) investigations were performed at 300 keV with a JEOL JEM 3010 electron microscope equipped with double-tilt holder, LaB_6 cathode, LINK ISIS EDS X-ray microanalysis and a backscattered electron-imaging device (BEI) coupled with STEM. AEM investigations were performed in TEM-EDS mode, with live counting time of 50 s and a nominal beam diameter of 25 nm. Recalculation and normalization of the AEM analyses were performed assuming the thin-film approximation, using experimental calibrations from silicate standards and expressed as 26 (O, OH) atoms per formula unit for $Ca_{10}(PO_4)_6(OH)_2$ apatite. Samples used for TEM–AEM investigations were from the same batches used for X-ray and SEM analysis and were gently crushed in a mortar under acetone, with a few drops of suspension deposited on a copper grid coated with a holy carbon film.

2.4. Crystallinity and crystal chemistry

Rietveld analysis used the fundamental parameter procedure implemented in TOPAS R (version 2.1) to extract phase content from the XRD patterns [43–45]. The HAp starting model used in the refinement was Holly Springs hydroxyapatite [46]. In each case, a background polynomial, scale factor, cell parameters, zero point correction and sample displacement were

refined. Atom positions, site occupancy factors and isotropic thermal parameters were fixed. Secondary phases were added as required using appropriate starting models (β-$Ca_3(PO_4)_2$ (β-TCP) [47], $CaCO_3$ (calcite) [48], CaO [49], and β-$Ca_2P_2O_7$ [50]) and the weight percent (wt%) of each Bragg diffracting phase, inclusive of the standard alumina, calculated from the refined scale factors [51].

2.5. Cadmium ion exchange

Macroporous HAp synthesized at 700 °C/6 h was immersed in a simulated waste liquor of cadmium nitrate containing 8×10^{-3} mol/l of Cd at temperatures from RT to 80 °C. In each case, the macroporous HAp was recovered after 100 h, washed thoroughly with distilled water, dried and the amount of Ca/Cd ions exchanged deduced by AEM.

3. Results and discussion

3.1. Macroscopic order

The 3DOM HAp products were white, rather than iridescent, indicating limited order at the millimeter scale, with SEM demonstrating that perfection was controlled by sintering temperature and time. Samples fired at 500 and 700 °C for 1 or 6 h retained their structural integrity over several microns while sintering at >800 °C for 1 h showed progressively more obvious decrepitation, although the macropores did not collapse totally even at 1000 °C (Fig. 1). Higher sintering temperatures enhanced crystallization and as a result pore diameters decreased from 1 to 0.8–0.9 μm. Complete removal of the polystyrene spheres required longer oxidation times and remnant polymer is apparent in the sample treated for 1 h at 700 °C (Fig. 1b), but clean pores are found after 6 h at 500 °C (Fig. 1a). The dominant arrangement of voids was confirmed as face-centered cubic by TEM (Fig. 2).

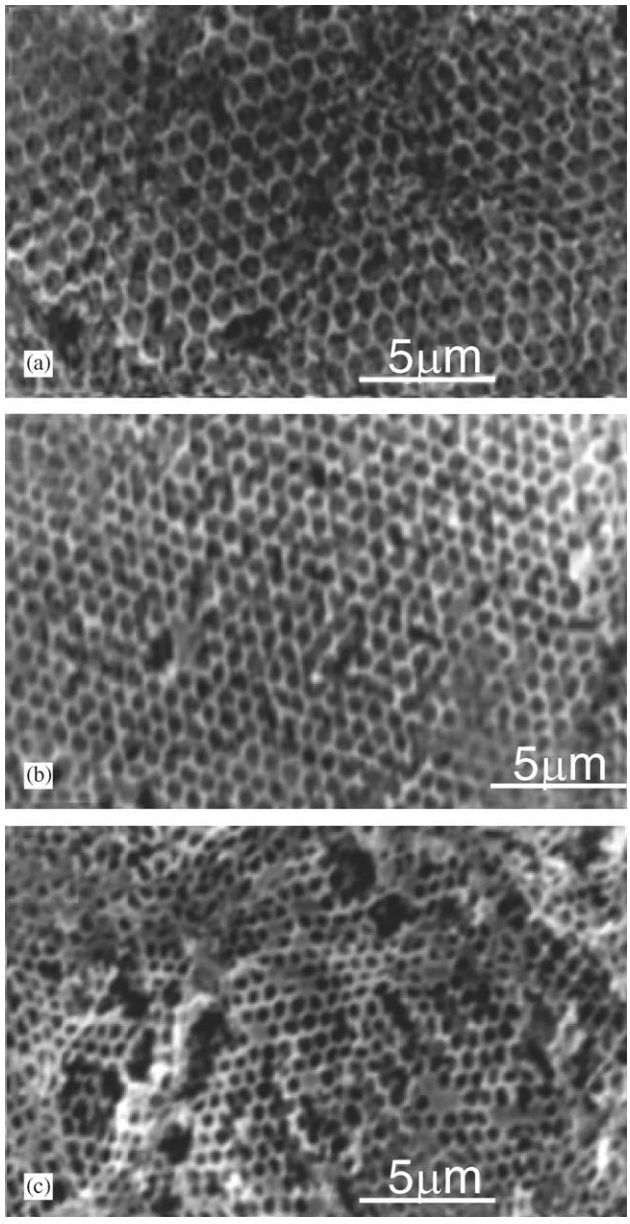

Fig. 1. Secondary electron images of macroporous HAp annealed at (a) 500 °C/6 h, (b) 700 °C/1 h, and (c) 900 °C/1 h.

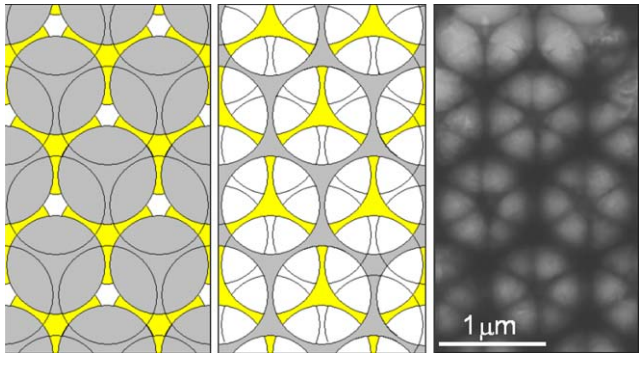

Fig. 2. From left to right, face centered close packed spheres viewed down [111]; corresponding void space characterized by 6-segments; and TEM image of macroporous HAp.

3.2. Wall chemistry and structure

Within the limited (±5%) precision of the AEM chemical analysis the 3DOM walls for all materials yielded a Ca:P ratio of 1.6 in accord with the expected stoichiometry of apatite. Wall thicknesses increased from ~9 to 25 nm in passing from 500 to 700 °C/6 h (Fig. 3b) due to densification and grain growth (Figs. 3a and b). At the highest temperatures the walls were assembled from large acicular HAp crystals (>200 nm in diameter) in similar orientations (Fig. 3c). Further inspection showed the crystals to be generally of prismatic habit with elongation along the apatite *c*-axis.

3.3. Phase development and amorphicity

A representative XRD profile obtained by Rietveld analysis of macroporous HAp containing standard alumina is shown for the sample sintered at 700 °C/6 h in Fig. 4. The relative wt% of crystalline phases (not taking into account the X-ray amorphous content) and absolute values (adjusted for the non-diffracting constituents) are presented in Table 1. HAp was the major crystalline phase in all the samples, with the relative yield from 500 to 1000 °C progressively increasing from 70% to 96%. It is well known that the synthesis of HAp powders by various solution methods is usually accompanied by the formation of calcium-phosphate and carbonate compounds [15,41,42,52–54]. In the present experiments, macroporous HAp coexisted with several minor phases including β-$Ca_3(PO_4)_2$ (β-TCP), $CaCO_3$ (calcite), β-$Ca_2P_2O_7$ (calcium pyrophosphate, CPP) and CaO (lime). Samples obtained at 500 and 700 °C/1 h contained β-TCP and calcite as impurity phases. However, above 700 °C these phases react to form HAp:

$$3Ca_3(PO_4)_2 + CaCO_3 + H_2O \rightarrow 2Ca_5(PO_4)_3OH + CO_2 \uparrow .$$

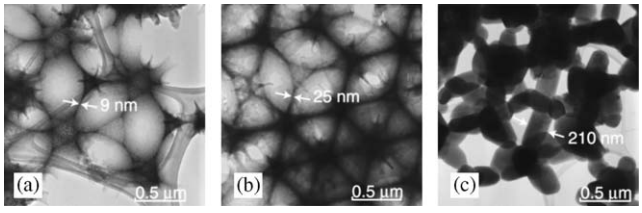

Fig. 3. TEM images comparing the crystalline wall thickness in samples synthesized for 6 h at (a) 500 °C, (b) 700 °C and (c) 1000 °C/1 h. Mottled contrast in (a) and (b) arises from aperiodic structure.

$CaCO_3$ and/or CaO were present as minor phases (< 3%) in all the samples even at the highest temperatures with mass balance considerations suggesting the HAp is slightly calcium deficient. Impurity peaks due to $Ca_2P_2O_7$ were only observed in samples sintered at the relatively low temperature of 500 °C consistent with its rapid conversion to HAp upon heating:

$$3/2\ Ca_2P_2O_7 + 2CaCO_3 + 1/2\ H_2O \rightarrow Ca_5(PO_4)_3OH + 2CO_2 \uparrow .$$

Longer sintering times achieved the same result as higher temperatures, with HAp yields increasing from 70% to 79% and 77% to 98% by calcining at 500 and 700 °C for 1 and 6 h, respectively with a corresponding

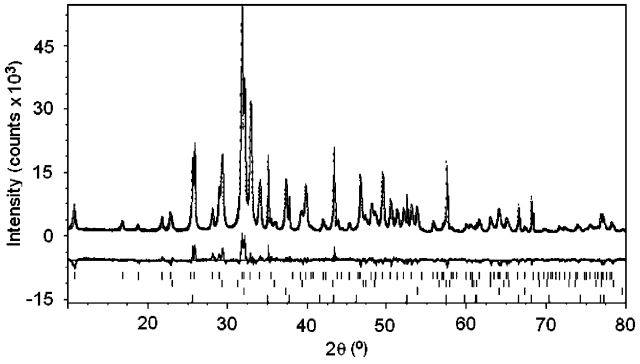

Fig. 4. Representative X-ray diffraction profile of macroporous HAp synthesized at 700 °C/6 h with corundum internal standard for calibration of amorphous content. Bragg reflection markers from top to bottom are HAp, calcite, β-TCP and corundum respectively. Phase proportions are summarized in Table 1.

Table 1
Phase development as a function of sintering time and temperature

Sintering temperature (°C)	Sintering time (h)	Weight percent (%)					
		X-ray crystalline phase					X-ray amorphous content
		$Ca_5(PO_4)_3OH$	β-$Ca_3(PO_4)_2$	$CaCO_3$	CaO	$Ca_2P_2O_7$	
500	1	70 (31)	8 (4)	19 (9)	—	3 (1)	(55)
700	1	77 (43)	3 (4)	20 (4)	—	—	(49)
800	1	89 (50)	—	10 (9)	1 (3)	—	(38)
900	1	97 (72)	—	1 (2)	2 (1)	—	(25)
1000	1	96 (82)	—	3 (3)	1 (1)	—	(14)
500	6	79 (52)	7 (4)	2 (2)	—	12 (7)	(35)
700	6	98 (81)	1 (3)	1 (2)	—	—	(14)

Crystalline phases are shown uppermost, while values corrected for the X-ray amorphous content are given in brackets.

Table 2
Crystallographic parameters of macroporous HAp

Sintering temperature (°C)	Sintering time (h)	Lattice parameters (Å)			Metaprism twist ϕ (°)	Cell volume (Å^3)	Crystallite size (nm)	R_b (%)
		a	*c*	*c*/*a*				
500	1	9.4139(10)	6.8997(9)	0.7329	24.75	529.5(1)	18	8.0
700	1	9.4207(5)	6.8933(4)	0.7317	24.05	529.8(1)	45	8.5
800	1	9.4200(10)	6.8914(8)	0.7316	24.12	529.6(1)	73	9.2
900	1	9.4205(6)	6.8816(4)	0.7305	24.07	528.9(1)	125	8.4
1000	1	9.4283(4)	6.8858(3)	0.7303	23.21	530.1(1)	198	9.2
Holly Springs Apatite [46]		9.424(4)	6.879(4)	0.730	23.1	529.1	—	—
500	6	9.4112(30)	6.8830(2)	0.7313	25.05	527.9(4)	30	8.2
700	6	9.4206(20)	6.8890(1)	0.7313	23.98	529.5(2)	60	9.4

reduction in β-TCP and calcite, verifying that these phases are intermediaries during apatite crystallization.

Substantial X-ray amorphous content was present in all materials (Table 1), as compared to fully dense HAp ceramic, since milder synthesis conditions are required to retain the macroporous structure. Another contributing factor may be that residual carbon is retained after burning off the polymer spheres. Although the carbon content was not analyzed it is noted that when sintering was continued for 6 h in oxygen the contribution from adventitious carbon is expected to be insignificant compared to X-ray amorphous inorganic phases. While the quantity of X-ray amorphous phase(s) decreases with increasing temperature, as it is consumed during HAp crystallization, it is noteworthy that even where HAp yield is highest, and the X-ray patterns display no obvious broad diffraction maximum indicative of amorphicity (Fig. 4), the measured values of non-diffracting content remain high (>14 wt%). X-ray amorphous material can be crystalline, but at a very fine scale recognizable only by TEM, however bright field images of 500 and 700 °C material show mottled contrast consistent with aperiodicity (Figs. 3a and b). The average crystallite size of HAp as determined from X-ray diffraction peak widths increased from 18 to 198 nm as sintering temperature was raised from 500 to 1000 °C in reasonable agreement with TEM observations (Table 2).

3.4. Infrared spectroscopy

FT-IR spectra of all materials (500–1000 °C) showed vibrational modes characteristic of PO_4^{3-} and OH^- groups in apatite (Fig. 5) [55,56]. The bands at 570 and 600 cm^{-1} were assigned to the O–P–O bending mode (ν_4), while the antisymmetric (ν_3) and symmetric (ν_1) stretching modes of P–O appeared at 1039/1090 and 960 cm^{-1}, respectively and the OH libration band was observed at 620 cm^{-1}. In addition a sharp band at 875 cm^{-1} and a broad band centered at 1425 cm^{-1} were present in samples sintered at 500 and 700 °C for 1 h.

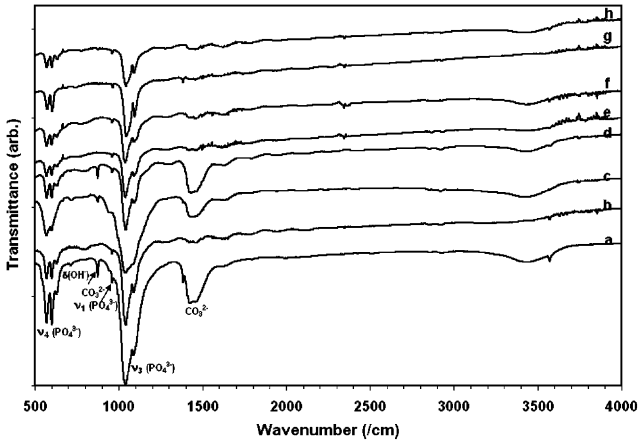

Fig. 5. FTIR (transmittance) spectra of macroporous apatite synthesized for 1 h at (a) 500 °C, (d) 700 °C, (f) 800 °C, (g) 900 °C, (h)1000 °C and for 6 h at (c) 500 °C, (e) 700 °C. (b) FTIR spectra of macroporous apatite obtained at 500 °C/1 h treated with dilute HCl.

These IR bands correspond to the stretching and bending modes of the carbonate (CO_3^{2-}) group [57–60] which disappeared after heat treatment above 700 °C. The carbonate band might arise from CO_3^{2-} ions that have replaced PO_4^{3-} sites in HAp or be due to $CaCO_3$ present as a secondary phase. As XRD had shown retained $CaCO_3$ in samples sintered at lower temperatures, and the carbonate band positions in calcite and carbonated apatite are similar, an unambiguous assignment of their origin was not directly possible.

However, as it is well known that $CaCO_3$ readily dissolves in dilute acids, macroporous apatite prepared at 500 °C/1 h and with the maximum $CaCO_3$ content (Table 1) was treated with dilute HCl, rinsed thoroughly with distilled water, dried and an IR spectrum of this powder collected. Comparing the IR spectra of the HCl-treated macroporous apatite (Fig. 5b) with the untreated one (Fig. 5a), it is seen that the finger print carbonate bands disappear after acid dissolution, indicating that the carbonate IR bands primarily arise from $CaCO_3$. Furthermore, the weight percent of $CaCO_3$ observed at temperatures above 700 °C is relatively low (Table 1)

and the characteristic CO_3^{2-} band at 1425 cm^{-1} in the IR spectra is absent (Figs. 5e–g). Taken together it is concluded that under all conditions the HAp is not carbonaceous to a significant extent.

3.5. HAp microporosity and nonstoichiometry

While hydroxyapatite is generally assigned the formula $Ca_{10}(PO_4)_6(OH)_2$ it is completely described in $P6_3/m$ by the unit cell content $[Ca_4^I][Ca_6^{II}][(PO_4)_6][OH]_2$ to emphasize two crystallographically distinct calcium sites. Although HAp is normally regarded as consisting of irregular polyhedra (aside from the phosphate groups) it has recently been shown that apatite crystal chemistry systematics can be simplified by emphasizing its microporous character [61]. In this description, channels are constructed from isolated PO_4 tetrahedra that are corner connected to Ca^IO_6 metaprism columns (Fig. 6). Although HAp has 1D channels approximately 5 Å in diameter, as distinct from the 3D channels in zeolites, it displays several zeolitic features including a framework which can be adjusted to accommodate different tunnel contents and an ability to accept large cations of different valance through the introduction of framework counter ions. HAp can be described formally using microporous nomenclature [62] as

$$|Ca^{I[16]}OH^{I[13]}|[Ca^{II[7]}P^{V[4]}O^{II[4]}]_p\{1[4^{12}12^2]\}.$$

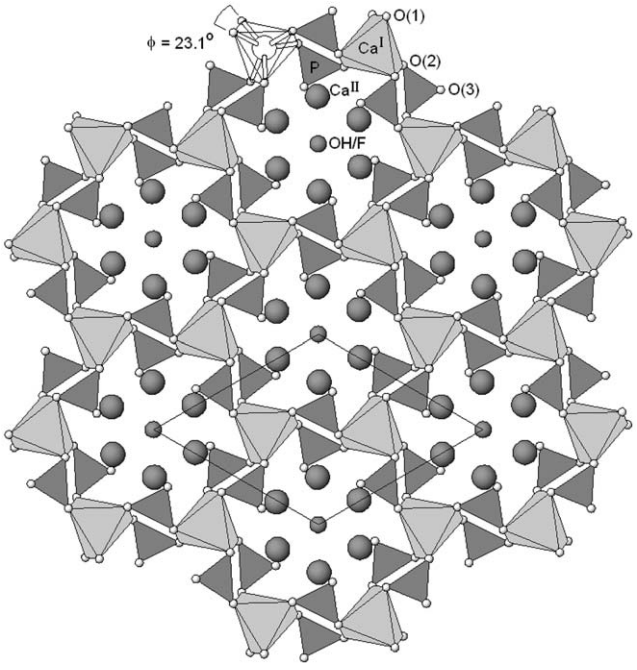

Fig. 6. Polyhedral representation of Holy Springs fluorohydroxyapatite viewed along [001] to emphasize the microporous character of the structure. The Ca^IO_6 metaprisms and PO_4 tetrahedra are highlighted to emphasize the co-operative movement of these corner-connected polyhedra as the metaprism twist angle (ϕ) varies to accommodate changes in channel occupancy.

Reversible ion exchange of the hydroxyl ion is well known (e.g. F, Cl, I), while more limited exchange of the Ca^{II} tunnel cations has been investigated (e.g. Cd, U, Ce) [63]. Unlike zeolites however, completely empty channels have not yet been reported.

While the tetrahedra are rigid units, the metaprisms can twist their (001) triangular faces through the angle ϕ with the magnitude of twist being a direct consequence of tunnel occupancy. Therefore, apatite may be considered a flexible 1D microporous compound with channels running parallel to [001] that dilate or contract in response to changes the size and extent of occlusion by cations and anions (Fig. 6) [64]. As the metaprism twist angle (ϕ) is an extremely sensitive probe of apatite composition, the corollary of this description is that HAp nonstoichiometry is established primarily by tunnel chemistry while the tunnel walls remain essentially stoichiometric [61].

The twist angle is related to the unit cell constants such that as ϕ decreases the tunnel diameter expands and the a-cell edge increases. For HAp an estimate of ϕ can be derived from the basal unit cell dimension a according to the relation

$$a = t\sqrt{13 - 28\sin^2\left(\frac{\phi}{4}\right) + 16\sin^4\left(\frac{\phi}{4}\right)},$$

where $t = 2.644$ Å is the average (001) equilateral triangle edge-length of the metaprism [64,65]. Using this approach it can be shown that for macroporous HAp samples fired for 1 h at increasing calcination temperatures (Table 2), the c/a ratio and ϕ decline simultaneously as the Ca^{II} channels become more completely filled (Fig. 7). In other words, HAp grows more nearly stoichiometric with Ca from residual $CaCO_3$ (calcite) migrating into the channel sites, and crystallographic parameters approaching those of near-stoichiometric Holly Springs hydroxy apatite. The introduction of additional calcium is also consistent with the overall dilation of unit cell volume. On the other hand, c is relatively insensitive to tunnel filling. During this process c decreases slightly, an effect tentatively ascribed to replacement of channel H_2O by OH according to the reaction

$$Ca^{II} + 2H_2O \rightarrow Ca^{II\,2+} + 2OH^-.$$

3.6. Ion exchange

Furuta et al. [22,25] demonstrated the removal of lead ions using porous HAp synthesized from gypsum wastes where the pore size distribution varied from 0.01 to 1 μm. Reichert and Binner [19] evaluated the heavy metal ion exchange of HAp ceramic foam filters and reported that ion adsorption rather than ion exchange

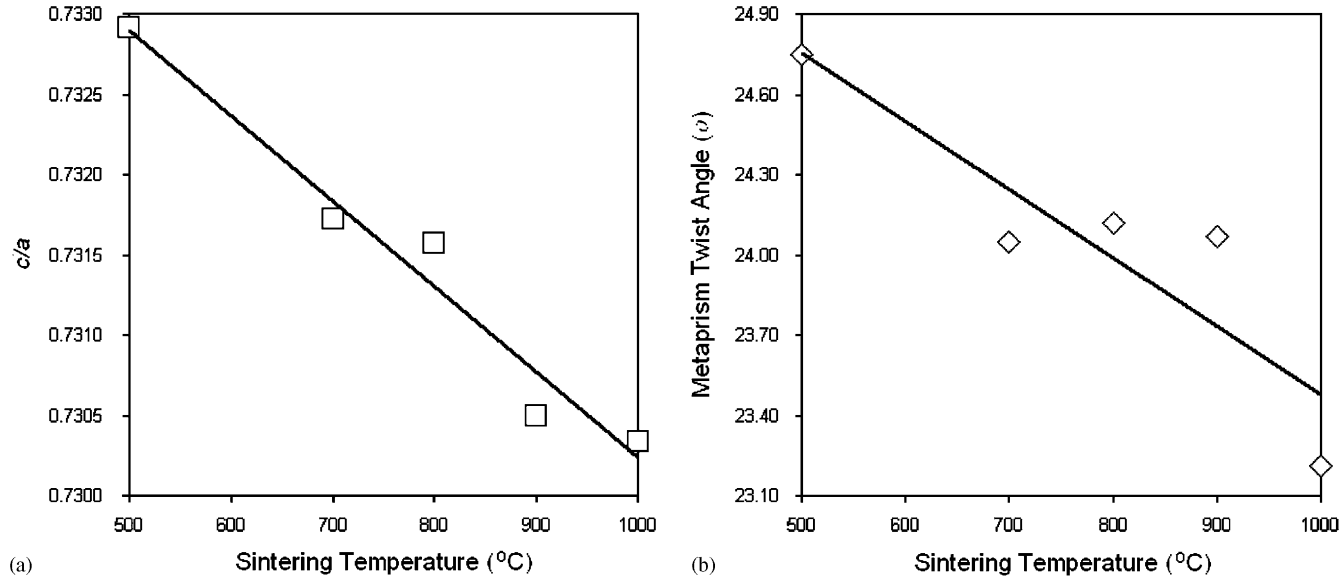

Fig. 7. Correlation of reduction in (a) c/a cell parameter ratio and (b) metaprism twist angle (ϕ). Errors are given in Table 2 and are smaller than the graphing symbols. Higher sintering temperatures result in more complete channel filling by calcium, a reduction in twist angle to accommodate the calcium, and the approach of HAp towards ideal stoichiometry.

was the predominant removal mechanism in these materials. 3DOM HAp with its membrane-like structure may effectively sieve the wastes and other impurities from waste water and simultaneously enhance ion-exchange reactions in the HAp walls, however the ion-exchange properties of apatite remain to be comprehensively demonstrated.

To test the potential of macroporous HAp as a permeable reaction barrier, the material synthesized at 700 °C/6 h was immersed in an 8×10^{-3} mol/l Cd solution [30,31]. Preliminary analysis by analytical TEM show homogeneous Ca/Cd ion exchange giving a macroporous wall composition of $Ca_{10-x}Cd_x(PO_4)_6(OH)_2$, with x increasing from 0.18 to 0.60 as the temperature was raised from RT to 80 °C. During the exchange reaction the macroporous framework remained intact and did not collapse after ion-exchange demonstrating the mechanical robustness of the structure. Detailed comparative Cd ion exchange studies on macroporous (3DOM) and powdered HAp have been performed with the results reported elsewhere [66]. The 3DOM macroporous HAp developed a smaller a-lattice parameter, as compared to its powdered counterpart, due to enhanced $Ca \leftrightarrow Cd$ exchange that resulted from the greater accessibility and shortened diffusion pathways provided by the porous network [66].

4. Conclusions

Near single-phase (98%) macroporous HAp with a pore size of 0.8–0.9 μm was synthesized, the yield increasing with longer firing times and higher temperatures. At lower temperatures, Ca-deficient HAp was predominant, however higher temperatures and/or extended calcinations consumed unreacted calcite, leading to more complete filling of the apatite microchannels, a reduction in metaprism twist angle ϕ, the dilation of the a cell edge and an approach to ideal stoichiometry. Crystal growth at higher temperatures exhibited a degree of self-assembly with single-crystal HAp wall segments forming. X-ray amorphous content was significant, especially at lower temperatures, and its role in facilitating grain growth and controlling functionality of the macropore walls remains under investigation. Preliminary cadmium ion-exchange experiments on macroporous HAp show homogeneous ion-exchange resulting in wall compositions of $Ca_{10-x}Cd_x(PO_4)_6(OH)_2$ with $0.18 < x < 0.30$ for $RT < T < 80$ °C suggesting these structures are suitable ecomaterials.

Acknowledgments

The authors would like to thank Dr. Jacques Plèvert for helpful discussions during the course of this work. This work was supported through the Agency for Science, Technology and Research, Singapore (A*STAR Grants 033 141 01 and 032 101 0023).

References

[1] B.T. Holland, C.F. Blanford, A. Stein, Science 281 (1998) 538–540.
[2] O.D. Velev, E.W. Kaler, Adv. Mater. 12 (2000) 531–534.

[3] C.F. Blanford, H. Yan, R.C. Schroden, M. Al-Daous, A. Stein, Adv. Mater. 13 (2001) 401–407.
[4] P.V. Braun, P. Wiltzius, Curr. Opin. Colloid Interface Sci. 7 (2002) 116–123.
[5] F. Meseguer, A. Blanco, H. Miguez, F.G. Santamaria, M. Ibisate, C. Lopez, Colloids Surf. A: Physicochem. Eng. Asp. 202 (2002) 281–290.
[6] Y. Xia, B. Gates, Y. Yin, Y. Lu, Adv. Mater. 12 (2000) 693–713.
[7] A. Stein, Microporous Mesoporous Mater 44/45 (2001) 227–239.
[8] A. Stein, R.C. Schroden, Curr. Opin. Solid State Mater Sci. 5 (2001) 553–564.
[9] O.D. Velev, A.M. Lenhoff, Curr. Opin. Colloid Interface Sci. 5 (2000) 56–63.
[10] B. Gates, Y. Yin, Y. Xia, Chem. Mater. 11 (1999) 2827–2836.
[11] S.H. Park, Y. Xia, Adv. Mater. 10 (1998) 1045–1048.
[12] M.A. Al-Daous, A. Stein, Chem. Mater. 15 (2003) 2638–2645.
[13] M.A. Carreon, V.V. Guliants, Chem. Mater. 14 (2002) 2670–2675.
[14] H. Yan, K. Zhang, C.F. Blanford, L.F. Francis, A. Stein, Chem. Mater. 13 (2001) 1374–1382.
[15] B.J. Melde, A. Stein, Chem. Mater. 14 (2002) 3326–3331.
[16] K. Zhang, H. Yan, D.C. Bell, A. Stein, L.F. Francis, J. Biomed. Mater. Res. 66A (2003) 860–869.
[17] R.C. Schroden, M.A. Daous, S. Sokolov, B.J. Melde, J.C. Lytle, A. Stein, M.C. Carbajo, J.T. Fernandez, E.E. Rodriguez, J. Mater. Chem. 12 (2002) 3261–3267.
[18] N. Arnich, M.C. Lanhers, F. Laurensot, R. Podor, A. Montiel, D. Burnel, Environ. Pollut. 124 (2003) 139–149.
[19] J. Reichert, J.G.P. Binner, J. Mater. Sci. 31 (1996) 1231–1241.
[20] S. Suzuki, T. Fuzita, T. Maruyama, M. Takahashi, Y. Hikichi, J. Am. Ceram. Soc. 76 (1993) 1638–1640.
[21] G. Lusvardi, G. Malavasi, L. Menabue, M. Saladini, Waste Manage. 22 (2002) 853–857.
[22] S. Furuta, H. Katsuki, S. Komarneni, J. Ceram. Soc. (Japan) 108 (2000) 315–317.
[23] S. Sugiyama, T. Ichii, M. Fujisawa, K. Kawashiro, T. Tomida, N. Shigemoto, H. Hayashi, J. Colloid. Interface Sci. 259 (2003) 408–410.
[24] Y. Xu, F.W. Schwartz, J. Contam. Hydrol. 15 (1994) 187–206.
[25] S. Furuta, H. Katsuki, S. Komarneni, J. Mater. Chem. 8 (1998) 2803–2806.
[26] Y. Watanabe, Y. Moriyoshi, Y. Suetsugu, T. Ikoma, T. Kasama, T. Hashimoto, H. Yamada, J. Tanaka, J. Am. Ceram. Soc. 87 (2004) 1395–1397.
[27] I.L. Shashkova, A.I. Ratko, N.V. Kitikova, Colloid Surf. A: Phys. Eng. Aspects 160 (1999) 207–215.
[28] E.V. Jones, K.V. Ragnarsdottir, A. Putnis, D. Bosbach, A.J. Kemp, G. Cressey, Chem. Geol. 151 (1998) 215–233.
[29] S. Sugiyama, H. Matsumoto, T. Ichii, H. Hayashi, Y. Hiraga, N. Shigemoto, J. Colloid Interface Sci. 238 (2001) 183–187.
[30] J. Jeanjean, S. McGrellis, J.C. Rouchaud, M. Fedoroff, A. Rondeau, S. Perocheau, A. Dubis, J. Solid State Chem. 126 (1996) 195–201.
[31] S. Mandjiny, K.A. Matis, A.I. Zouboulis, M. Fedoroff, J. Jeanjean, J.C. Rouchaud, N. Toulhoat, V. Potocek, C. Loos-Neskovic, P. Maireles-Torres, D. Jones, J. Mater. Sci. 33 (1998) 5433–5439.
[32] S. McGrellis, J.N. Serafini, J. Jeanjean, J.L. Pastol, M. Fedoroff, Sep. Purif. Tech. 24 (2001) 129–138.
[33] J.J. Middelburg, R.N.J. Comans, Chem. Geol. 90 (1991) 45–53.
[34] M. Fedoroff, J. Jeanjean, J.C. Rouchaud, L. Mazerolles, P. Trocellier, P. Maireles-Torres, D.J. Jones, Solid State Sci. 1 (1999) 71–84.
[35] F.M. Rivera, S. Masset, J. Dumonceau, M. Fedoroff, J. Jeanjean, J. Mater. Sci. Lett. 18 (1999) 1143–1145.
[36] W.P. Reed, Certificate SRM 676, National Institute of Standards and Technology (NIST) Gaithersburg, MD 20899, 1992.
[37] A.G. De La Torre, S. Bruque, M.A.G. Aranda, J. Appl. Crystallogr. 34 (2001) 196–202.
[38] R.S. Winburn, Proceedings of the 51st Annual Conference on Application of X-ray Analysis, Advances in X-ray Analysis, USA, vol. 46, 2002, pp. 210–219.
[39] F. Guirado, S. Gali, S. Chinchon, Cement Concrete Res. 30 (2000) 1023–1029.
[40] P.S. Whitfield, L.D. Mitchell, J. Mater. Sci. 38 (2003) 4415–4421.
[41] X. Orlhac, C. Fillet, P. Deniard, A.M. Dulac, R. Brec, J. Appl. Cystallogr. 34 (2001) 114–118.
[42] T.E. Gills, Certificate SRM656, National Institute of Standards and Technology (NIST) Gaithersburg, MD 20899, 1995.
[43] R.A. Young (Ed.), The Rietveld Method, Oxford University Press, Oxford, 1993.
[44] R.W. Cheary, A.A. Coelho, J. Appl. Crystallogr. 31 (1998) 851–861.
[45] A.F. Gualtieri, J. Appl. Crystallogr. 33 (2000) 267–278.
[46] K. Sudarsanan, R.A. Young, Acta Crystallogr. B 25 (1969) 1534–1543.
[47] L.A. Schroeder, B. Dickens, W.E. Brown, J. Solid State Chem. 22 (1977) 253–262.
[48] S.A. Markgraf, R.J. Reeder, Am. Miner. 70 (1985) 590–600.
[49] C.H. Shen, R.S. Liu, J.G. Lin, C.Y. Huang, Mater. Res. Bull. 36 (2002) 1139–1148.
[50] N.C. Webb, Acta Crystallogr. 21 (1966) 942–948.
[51] R.J. Hill, C.J. Howard, J. Appl. Crystallogr. 20 (1987) 467–474.
[52] S. Koutsopoulos, J. Biomed. Mater. Res. 62 (2002) 600–612.
[53] N. Rangavittal, A.R. Landa-Canovas, J.M. Gonzalez-Calbet, M. Vallet-Regi, J. Biomed. Mater. Res. 51 (2000) 660–668.
[54] P. Layrolle, A. Ito, T. Tateishi, J. Am. Ceram. Soc. 81 (1998) 1421–1428.
[55] J.C. Elliott, Structure and Chemistry of the Apatites and Other Calcium Orthophosphates, Elsevier, Amsterdam, 1994.
[56] T.A. Kuriakose, S.N. Kalkura, M. Palanichamy, D. Arivuoli, K. Dierks, G. Bocelli, C. Betzel, J. Cryst. Growth 263 (2004) 517–523.
[57] F. Apfelbaum, H. Diab, I. Mayer, J.D.B. Featherstone, J. Inorg. Biochem. 45 (1992) 277–282.
[58] W.G. Perdok, J. Christoffersen, J. Arends, J. Cryst. Growth 80 (1987) 149–154.
[59] N.V. Vagenas, A. Gatsouli, C.G. Kontoyannis, Talanta 59 (2003) 831–836.
[60] M.A. Legodi, D. de Waal, J.H. Potgieter, S.S. Potgieter, Miner. Eng. 14 (2001) 1107–1111.
[61] T.J. White, C. Ferraris, J.Y. Kim, S. Madhavi, Apatite—An adaptive framework structure, in: G. Ferraris, S. Merlino (Eds.), Reviews in Mineralogy and Geochemistry, vol. 57, The Mineralogical Society of America, Washington, 2005, pp. 307–402 (Chapter 10).
[62] L.B. McCluster, F. Liebau, G. Engelhardt, Pure Appl. Chem. 73 (2001) 381–394.
[63] J. Wright, B. Hansen, J. Conca, J. Contam. Hydrol. (in press 2005).
[64] T.J. White, Z.L. Dong, Acta Crystallogr. B 59 (2003) 1–16.
[65] Z.L. Dong, T.J. White, Acta Crystallogr. B 60 (2004) 146–154.
[66] S. Madhavi, C. Ferraris, T.J. White, Environ. Sci. Technol. (2005), submitted for publication.